2005－CVIM－149（33）
2005／5／13

インバースレンダリングに基づく物体表面反射特性の密な推定

町田 貴史† 横矢 直和‡ 竹村 治雄†

†大阪大学　サイバーメディアセンター
‡奈良先端科学技術大学院大学　情報科学研究科

あらまし:　実環境に仮想物体を合成表示する複合現実感の研究において，より写実性の高い表現を行うために現実物体を仮想化する仮想化現実の研究が盛んに行われている．特に，物体の表面反射特性を推定することは実環境と仮想化された物体との間の陰影矛盾を解決するために重要である．この問題に対して我々は，物体の距離画像と表面のテクスチャ画像から物体の反射特性を密に推定する研究を行ってきた．また複雑な形状を有する物体に関しては，物体表面上での二次反射による相互反射の影響を考慮した手法を提案してきた．しかし，鏡面反射成分による相互反射の影響が除去できないという問題があった．本報告では，物体表面における反射特性の推定についてインバースレンダリングの観点から３つの反射特性の推定法を提案する．具体的には物体表面の反射成分の密な観測を基にし，鏡面反射成分の密な推定，さらに拡散反射や鏡面反射を含む相互反射の影響を考慮して反射特性を推定する手法について報告する．実験では，推定された反射特性を従来法と比較することで，様々な仮想環境内の照明条件に対して忠実に物体を表現できることを示す．

Dense Estimation of Surface Reflectance Properties Based on Inverse Rendering

Takashi Machida† Naokazu Yokoya‡ Haruo Takemura†

†Cybermedia Center, Osaka University
‡Graduate School of Information Science, Nara Institute of Science and Technology

Abstract:　In augmented virtuality, it is important to estimate object surface reflectance properties to render objects under arbitrary illumination conditions. There exist a number of methods to estimate reflectance properties of object surfaces densely. However, it was difficult to estimate surface reflectance properties faithfully for objects with interreflections. This paper describes a new method for densely estimating non-uniform surface reflectance properties of real objects constructed of convex and concave surfaces with diffuse and specular interreflections. We use registered range and surface color texture images obtained by a laser rangefinder. The proposed method first determines positions of light to take color images for discriminating diffuse and specular reflection components of surface reflection. Surface reflectance parameters are then estimated based on an inverse global illumination rendering. Experiments show the usefulness of the proposed method.

1 Introduction

Computer graphics(CG) is being increasingly used to visualize real objects and environments. Applications in entertainment, architecture, interior design, virtual reality, and digital museums often require that aspects of the real world be rendered realistically from novel viewpoints and/or under novel illumination. In addition, augmented reality (AR) technologies have been developed. These techniques need that a virtualized object is seamlessly merged into the real world [1].

In order to represent a virtualized object photorealistically, there is an approach which is called *inverse rendering*. To produce a photorealistic image, the object geometry, reflectance properties and lighting effect in a scene are required. In the fields of computer vision and graphics, many researches has developed to estimate each information from images in the scene or objects. Especially, it is important to estimate an object surface reflectance properties [17, 16, 18]. This report focuses on the estimation of the object reflectance properties based on *inverse rendering*. This approach, which is sometimes referred to as *inverse reflectometry*, reproduces the object shape and surface reflectance properties. If the object surface reflectance properties are estimated at once, the virtualized object can

be rendered appropriately under virtualized illumination conditions estimated from real environments [29, 24, 2, 7, 11, 13, 12, 15, 25]. In these methods, surface reflectance models with several parameters are employed, and shape and color information of the object are used to estimate the reflectance parameters. In this thesis, estimation of object surface reflection in *inverse rendering* framework is focused.

In some works [2, 7, 15] for *Inverse Local Rendering*, it is assumed that an object has a uniform reflectance property over the entire surface. Reflectance parameters are estimated by using the standard least-squares method to fit a reflectance model to a given color image. Due to the assumption, such methods cannot be applied to objects which consist of several different materials and have non-uniform reflectance properties. On the other hand, to treat non-uniform surface objects, some works have used multiple images of an object under different lighting conditions and have estimated reflectance parameters by solving simultaneous equations [11, 13, 12]. However, such methods still have a problem such that results are not stable especially when the specular reflection component is very small. Sato et al. [25] have developed a methodology to estimate non-uniform reflectance properties. Although the method can be applied to objects with non-uniform reflectance properties, the shape of object should be limited. This is because it is difficult to observe the specular reflection component over the entire surface, since the lighting condition for a pose of the object against the camera cannot be changed in the method.

Inverse Local Rendering can estimate the object surface reflectance properties based on only direct illumination effect. However, in the real world, the object has interreflections. Therefore, we must estimate the reflectance properties with considering interreflections on the surface. For solving this problem, Fournier et al. [6] have originally developed a method for estimating surface reflectance properties using the radiosity method in an indoor scene. This method assumes uniform reflectance on an object surface and determines only the diffuse reflectance parameter. There are some attempts to estimate both diffuse and specular reflectance properties of a room [3, 14]. They, however, also assume that all objects have the uniform reflectance properties in the segmented region, therefore, their algorithm cannot be also applied to an object which has non-uniform surface reflectance properties. Yu et al. [29] have estimated surface reflectance properties of a room from color and geometry data considering both diffuse and specular interreflections based on the inverse global illumination rendering. They employ a hybrid rendering method which combines the radiosity and Monte Carlo ray tracing method. Boivin et al. [3] have also attempted to estimate surface reflectance properties with considering diffuse interreflections. These methods assume that the surface of interest has uniform reflectance properties. Therefore their algorithms cannot be applied to an non-uniform surface reflectance object.

In this study, we focus on estimating non-uniform surface reflectance properties based on *inverse rendering* framework as mentioned previously. We first propose a method for estimating local surface reflectance properties. For this purpose, we select optimum light positions in order to observe both diffuse and specular reflection on the object surfaces. By this process, we can decompose diffuse and specular components at each surface point. Then, we densely estimate the object surface reflectance properties based on *Inverse Local Rendering*. Moreover, we propose two estimation methods which are categorized in *Inverse Global Rendering*. One is based on radiosity rendering method and Torrance-Sparrow reflectance model. The other is based on photon mapping rendering method. The former method can estimate diffuse reflectance parameter by calculating inverse radiosity algorithm and specular and surface roughness parameter by calculating inverse local reflectance model. The advantage of this method is that the diffuse interreflection can be considered [20, 19, 21]. In the inverse radiosity method, the influence of the specular interreflections still remains.

To solve the problem which the inverse radiosity estimation method can not cope with, we proposed the latter method which can also estimate diffuse reflectance, specular reflectance and the surface roughness parameters. In this method, because both diffuse and specular interreflections can be considered, the inverse photon mapping method is more efficient estimation method with comparing to the conventional methods. In addition, because photon mapping rendering method recently implemented on a graphics hardware(GPU)[23, 22], it is desired that the real-time estimation of the object reflectance parameters.

Finally, in experiments, the three proposed methods are qualitatively and quantitatively evaluated with reflectance parameter estimation and virtual relighting. Three methods are compared with each other, and *Inverse Global Rendering* is also useful for estimating the object surface reflectance properties. The radiosity method and the photon mapping method can usually be applied to a closed environment. However, we experimentally verify that the inverse radiosity and the inverse photon mapping can also be applied to an open environment in which the influence of the environment light is negligible.

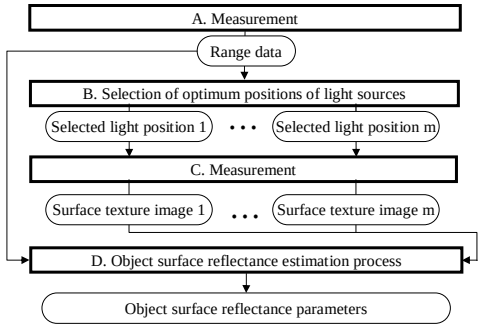

Figure 1: General flow diagram of surface reflectance modeling in this study.

2 Dense Observation of Reflection Components

Figure 1 illustrates a flow diagram of our light selection (A, B, C) and object surface reflectance estimation (D) processes. This section focusses on the light selection process. We use a laser rangefinder to obtain a range and a surface color images, and then select optimum light positions based on the object range image. Here, the surface reflectance estimation process (D) is described in the next section. Our light selection process consists of two parts: measurement of an object (A, C) and selection of light sources (B). In the followings describe the overview of the light selection process.

1. Measurement of 3D geometry and surface texture
   An object shape is acquired with a laser rangefinder in a dark room. Multiple surface texture images are also obtained under different light sources whose positions are selected in the process (B).

2. Preprocessing
   Generally, a range image which is acquired by the laser rangefinder has some noises including quantization errors. Moreover, there is a problem such that a normal vector can not be correctly calculated in the vicinity of discontinuities. Therefore, we remove noises and locally fit quadratic surfaces to the range image to acquire the normal vector correctly.

3. Selection of light source
   According to the object shape and the position of the camera, multiple light positions are selected among a number of possible positions of the light source to measure both diffuse and specular reflection components densely on the object surface.

We describe the detail of optimum light position selection method in the following sections.

2.1 3D measurement of object and Preprocessing

We use a laser rangefinder (Cyberware 3030RGB) with known positions of point light sources and a camera for acquiring range and surface color images, which is located in a dark room as shown in Figure 2(a). This system can simultaneously obtain registered range and surface color texture images rotating the rangefinder and the camera around an object. Figure 2(b) shows the illustration viewed from the top of the device. The camera is located at $X1$ and a texture image is acquired through mirrors located at $X2$ and $X3$. We thus can assume that the camera is virtually located at $X4$ and the camera looks toward the center of rotation.

Generally, the noise and quantization errors are included in the range image acquired from the laser rangefinder. There is also a problem that the surface normal is not calculated accurately around the discontinuity in the range image. Therefore, we employ an adaptive local quadratic surface fitting [28] as a preprocessing.

2.2 Selection of positions of light sources based on reflectance model

Here, we address the problem of determining light source positions for effectively observing both diffuse and specular reflection components on an object surface. In the present experimental setup, multiple positions of a light source are determined among 60 possible positions prepared around the laser rangefinder and these are two-dimensionally arranged at the interval of 5 cm as shown in Figure 3. After optimum light positions are selected, a single light source is attached at the selected positions in turn so that the calibration of brightness among multiple lights is not needed. Note that the position of a camera is cal-

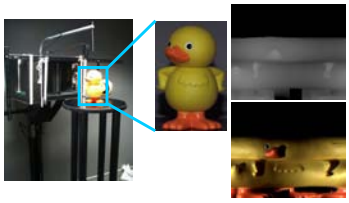

(a) Apparance of 3D-Digitizer

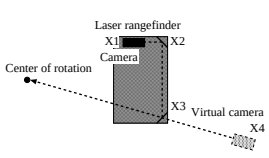

(b) Direction of camera in laser rangefinder.

Figure 2: 3D-Digitizer in experimental setup.

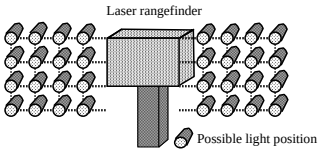

Figure 3: Multiple possible light source positions.

ibrated in advance by measuring a calibration box whose size is known. The position of a light source is also calibrated based on the distance from the center of rotation in the world coordinate. In addition, we can ignore the influence of environmental light because the object is measured in a dark room.

Let I_p be a color image which is to be obtained with a possible light position p ($p = 1, \cdots, 60$) and consists of γ pixels $(i_{p1}, \cdots, i_{p\gamma})$, where i_{px} means a color intensity with corresponding to the surface point x, D_p be the number of pixels which include only the diffuse reflection component in I_p, and S_p be the number of pixels which include the strong specular reflection in I_p.

First, the following conditions are examined for each pixel in the object surface texture under each light position p.

- **Measurability of light reflection**
- **Measurability of only diffuse reflection**
- **Measurability of strong specular reflection**

Second, the light positions p and q which satisfy $D_p = Max(D_1, \cdots, D_{60})$ and $S_q = Max(S_1, \cdots, S_{60})$ are selected. In the next light source position selection, the position which satisfies the same condition is selected among the rest except for light source positions decided so far. Then, m light positions are selected to densely estimate reflectance parameters. The selection of light positions is repeated until almost all pixels are observed once for only the diffuse reflection component and twice for the strong specular reflection component.

We introduce a threshold th_1, i.e., the ratio of the measurability of both reflection components to stop the process of selecting light positions. With respect to determining the threshold th_1, we judge the ratio of the measurability of the specular reflection with all possible positions. This ratio is a limit of measuring the specular reflection component. Using the threshold, we can terminate the light selection process in the case that the ratio of measurability of specular reflection component cannot increase more, even if the number of positions of light source is increased. In such a way, reflectance parameters can be efficiently estimated almost the whole object surface using a limited number of texture images. In the following, the three measurability conditions above are described in detail, after giving the surface reflection model employed in the present study.

2.2.1 Torrance-Sparrow model

For selecting the optimum light positions among possible light positions, we need to judge whether a pixel in the image taken by a laser rangefinder has each reflection component. Here, there is a surface reflection model which represents the property of both diffuse and specular reflection components. The reflection model describes the direction of reflection from a light source based on an object geometry, a viewing direction and a light source direction. If these parameters are known, we can judge whether each pixel in the image has both reflection components. In this section, we employ the Torrance-Sparrow model [26] to represent local surface reflections physically. The Torrance-Sparrow model is given as:

$$i_x = \frac{Y}{C^2}\{P_{dx}\cos\theta_{dx} + \frac{P_{sx}}{\cos\theta_{vx}} exp(-\frac{\theta_{rx}^2}{2\sigma_x^2})\}, \quad (1)$$

where i_x represents an observed intensity with corresponding to the surface point x, i_{dx} and i_{sx} denote the diffuse and specular reflection components, C is an attenuation coefficient concerning the distance between a point light source and an object surface point, Y represents the strength of a light source. P_{dx}, P_{sx} and σ_x are the diffuse reflectance, the specular reflectance and the surface roughness parameters which is the standard deviation of a Gaussian distribution, respectively. θ_{dx} is an angle between a light source vector $\mathbf{L}_x$ and a surface normal vector $\mathbf{N}_x$, θ_{vx} is an angle between a viewing vector $\mathbf{V}_x$ and a surface normal vector $\mathbf{N}_x$, and θ_{rx} is an angle between a surface normal vector $\mathbf{N}_x$ and a half vector $\mathbf{R}_x$. Note that the half vector $\mathbf{R}_x$ means halfway between a light vector $\mathbf{L}_x$ and a viewing vector $\mathbf{V}_x$, and is given by Equation (1). All vectors are unit vectors. Figure 4 illustrates the geometry for this model. θ_{rx} is used for judging whether the specular reflection occurs or not.

To densely estimate non-uniform surface reflectance parameters independently, it is required to observe each surface point x under at least three different lighting conditions: One for determining one unknown parameter P_{dx} and others for acquiring the remaining two unknown parameters P_{sx} and σ_x. The selection of optimum positions of the light source in Figure 1(B) is repeated until almost all pixels satisfies three different lighting conditions[17]. As a result of this process, a certain number of light positions, say m (as described previously) are selected to densely observe both diffuse and specular reflection components.

A texture image is obtained with a selected light position p ($p = 1, \cdots, m$) and consists of γ pixels

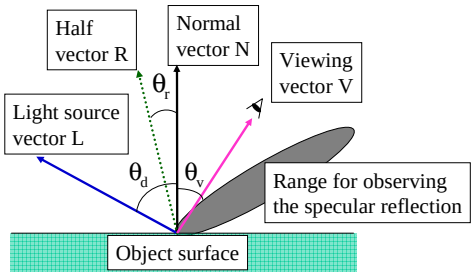

Figure 4: Diffuse and Specular reflection on an object surface.

$(i_{p1}, \cdots, i_{p\gamma})$, where i_{px} means a color intensity of a surface point x.

2.2.2 Measurability of light reflection

In order to measure the light reflection at a specific point x of the object surface, the surface point must be observable from the camera position and the light must illuminate the surface point. Thus the positional relationship among the camera, the point and the light source must satisfy the following conditions.

$$(\mathbf{V}_x \cdot \mathbf{N}_x) > 0, \ (\mathbf{L}_{px} \cdot \mathbf{N}_x) > 0, \tag{2}$$

where $\mathbf{V}_x$, $\mathbf{L}_{px}$, and $\mathbf{N}_x$ are the viewing direction, the light source direction, and the surface normal with corresponding to the surface point x, respectively. Note that the viewing direction $\mathbf{V}_x$ and the surface normal $\mathbf{N}_x$ are independent of the light source position p.

Even when the above equations are both satisfied, there is a possibility that a shadow is casted on the pixel. In this case, the pixel must not be used for estimating reflectance parameters. Whether a surface point x is covered by a shadow casted by light source p or not can be judged by the conventional method [5].

2.2.3 Measurability of diffuse reflection only

When the pixel at the surface point x exhibits only the diffuse reflection, the half vector $\mathbf{R}_{px}$ satisfies the following equation.

$$\theta_{rx} = cos^{-1}(\mathbf{N}_x \cdot \mathbf{R}_{px}) > \theta_{th1}, \tag{3}$$

where θ_{th1} is a threshold angle between $\mathbf{N}_x$ and $\mathbf{R}_{px}$. Equation (3) implies that only the diffuse reflection component is observed if θ_{rx} is greater than θ_{th1} as illustrated in Figure 5. When this condition stands and the pixel is not in a shadow, the pixel is judged to have diffuse reflection only and is counted in D_p.

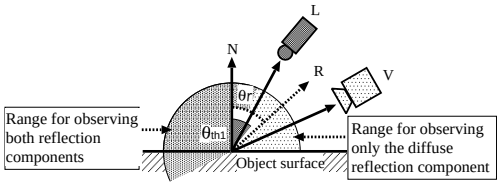

Figure 5: Observation of only the diffuse reflection.

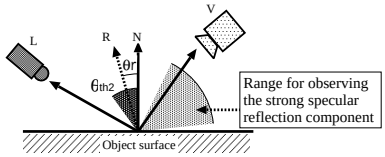

Figure 6: Observation of the specular reflection.

2.2.4 Measurability of strong specular reflection

When the pixel at the surface point x exhibits the strong specular reflection, the half vector $\mathbf{R}_{px}$ satisfies the following equation.

$$\theta_{rx} = cos^{-1}(\mathbf{N}_x \cdot \mathbf{R}_{px}) \leq \theta_{th2}, \tag{4}$$

where θ_{th2} is a threshold angle between $\mathbf{N}_x$ and $\mathbf{R}_{px}$. Equation (4) means that both the diffuse and specular reflection components are observed if θ_{rx} is smaller than θ_{th2} as illustrated in Figure 6. The above condition is based on the fact that the specular reflection is observed strongly in a limited range of viewing angle. When this condition stands and the pixel is not in a shadow, the pixel is judged to have strong specular reflection and is counted in S_p.

2.3 Experimental results

We experimentally demonstrate the results of efficiently selecting optimum light positions from dense set of possible light positions. We then show the actual measurability of both diffuse and specular reflection components on test objects. Four objects are used in experiments (Figure 7). Object A and B have non-uniform reflectance properties with respect to both diffuse and specular reflection, and have comparatively complicated geometry. These objects are mainly used to verify that our proposed methods can estimate the object with non-uniform reflectance properties in Section 3 and eliminate the influence of interreflections in Section 4. Object C and D have non-uniform diffuse reflectance and uniform specular reflectance properties. These objects are also mainly used to verify that our proposed methods can eliminate both diffuse and specular interreflections in Sec-

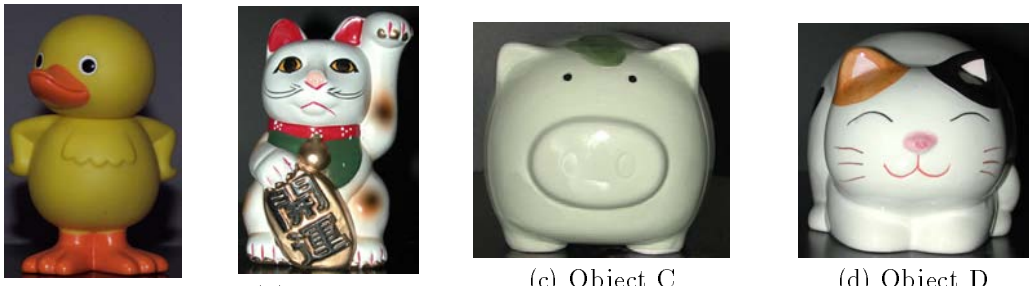

(a) Object A (b) Object B (c) Object C (d) Object D

Figure 7: Four objects used in the experiment.

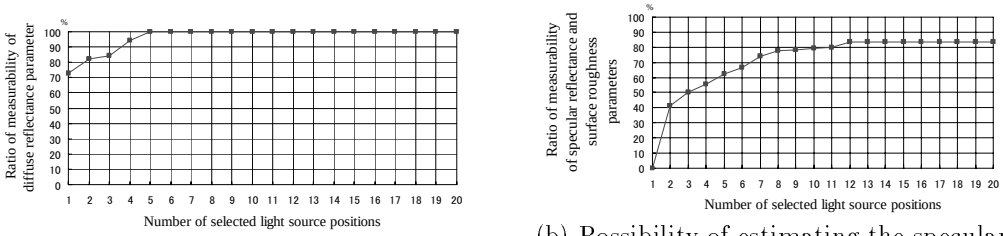

(a) Possibility of estimating the diffuse reflectance parameter

(b) Possibility of estimating the specular reflectance and the surface roughness parameters

Figure 8: Measurability of both reflection components for Object A.

Table 1: Measurability of both reflection components and the number of selected light sources for estimating the reflectance parameters of Objects A, B, C and D.

Measurement object	Object A	Object B	Object C	Object D
Number of selected light positions	12(5)	14(4)	10(3)	9(4)
Diffuse reflection component	100.0%	100.0%	100.0%	100%
Specular reflection component (with our method)	83.46%	91.02%	89.17%	91.72%
Specular reflection component (with 60 light positions)	83.52%	93.56%	91.27%	94.90%

tion 5. According to Ward et al.[27], the strong specular component can be observed within 20 degree around a half vector $\mathbf{R}$. Therefore, the thresholds $\theta_{th1} = 60^o$, $\theta_{th2} = 20^o$, $th_1 = 80\%$ are fixed. In addition, standard conventional PC (CPU: 3.06GHz, Memory: 1GB) is used in all of the experiments.

Figure 8 illustrates the measurability of both reflection components with respect to the number of light sources for objects A. The vertical axis means the measurability of diffuse or specular reflection component and the horizontal axis means the number of selected light sources in our light selection algorithm. Note that the horizontal axis only extends to 20, because these graphs do not change even if all 60 possible positions are used. (a) shows the relation between the number of selected light position and the ratio of measurability of diffuse reflection component. For example, when the number of selected light source positions is five, the ratio of the measurability of the diffuse reflection component is 100%. On the other hand, (b) shows the relation between the number of selected light positions and a radio of measurability of specular reflection component. Even when Object A is measured at all possible positions, the ratio of the measurability of the specular reflection component is 83.53%. In the proposed method, the ratio of measurability of the specular reflection component is 83.46% with 12 automatically selected light source positions. The measurability of both reflection components and the number of selected light sources for estimating reflectance parameters of Objects A, B, C and D are summarized in Table 1. The number in brackets indicates the number of selected light source positions required to estimate the diffuse reflectance

parameter. This table also shows a comparison of our light selection method and the case of using all possible positions with respect to the measurability of specular reflection component. It is shown that the specular reflection component is observed in all objects using a limited number of light source positions efficiently compared with using all 60 possible positions.

3 Inverse Local Rendering for Dense Reflectometry Estimation

The following section describes *how to estimate* the object surface reflectance properties densely using the Torrance-Sparrow model. Note that because the Torrance-Sparrow model supports non-metal and heterogeneous dielectric material, we can not estimate the object surface reflectance properties with metaric material. In addition, although the Torrance-Sparrow model supports fresnel component, we ignore the fresnel component because it is assumed that the object is opaque. The mirror material is not also supported.

3.1 Estimation of surface reflectance parameters

Let $I_{p,diff}$ be the set of pixels which consist of only the diffuse reflection component with possible light position p and consists of γ pixels $(i_{p,d1}, \cdots, i_{p,d\gamma})$, where $i_{p,dx}$ means a color intensity with corresponding to the surface point x. If it is judged that $i_{p,dx}$ does not consist of only the diffuse reflection component, $i_{p,dx} = 0$. Let $I_{p,both}$ be the set of pixels which include the specular reflection component strongly, and also consists of γ pixels $(i_{p,b1}, \cdots, i_{p,b\gamma})$, where $i_{p,bx}$ means a color intensity on the object surface point x. If it is judged that $i_{p,bx}$ does not include the strong specular reflection component, $i_{p,bx} = 0$. In addition, T_{diff} means a pixel containing only the diffuse reflection component and T_{spec} means a pixel containing strong specular reflection component. T_{none} means a pixel which is classified into neither T_{diff} nor T_{spec}. Each pixel is classified into three types T_{diff}, T_{spec} and T_{none}.

3.1.1 Estimation of diffuse reflectance parameter

The estimation process is performed at each point on the object surface. Pixels in multiple images with corresponding to the object surface are used as shown in Figure 9. The diffuse reflectance parameter P_{dx} at surface point x is estimated by solving the following equation from Equation (1).

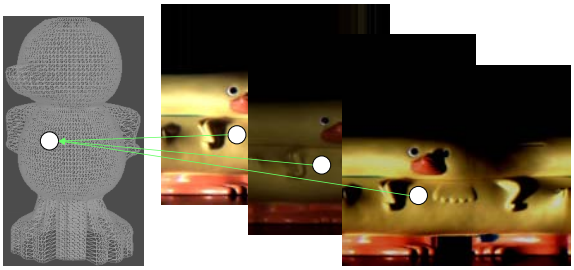

Figure 9: The object point in multiple texture images.

$$P_{dx} = \frac{C^2 i_{p,dx}}{Y \cos\theta_{dx}}, \tag{5}$$

where $i_{p,dx}$ is the value of the pixel at surface point x in the image $i_{p,dx}$. $\cos\theta_{dx}$ is calculated from surface normal vector $\mathbf{N}_x$ and light source vector $\mathbf{L}_{px}$. In order to get the most reliable estimation, the pixel whose angle θ_{rx} is the smallest but greater than θ_{th1} is selected.

3.1.2 Estimation of specular reflectance and surface roughness parameters

The specular reflectance parameter P_{sx} and surface roughness parameter σ_x at surface point x are also estimated by solving Equation (1) with $\mathbf{N}_x$, $\mathbf{L}_{px}$, $\mathbf{V}_x$ and the value of the specular reflection component which is extracted from the pixels $i_{p,bx}$ and $i_{q,bx}$ in the images $I_{p,both}$ and $I_{q,both}$. In order to get the most reliable estimation, the pixels whose angle θ_{rx} are the smallest or the second smallest and are smaller than θ_{th2} are selected.

First, the diffuse reflection component is computed with the diffuse reflectance parameter P_{dx} estimated above and Equation (1). Second, the specular reflection component is extracted by subtracting the diffuse reflection component.

$$\begin{cases} i_{p,sx} = i_{p,bx} - i_{p,dx} \\ i_{q,sx} = i_{q,bx} - i_{q,dx} \end{cases} \tag{6}$$

Finally, the specular reflectance and surface roughness parameters are obtained by the following equations.

$$\begin{cases} i_{p,sx}\cos\theta_{vx} = P_{sx} \cdot exp(-\theta_{rx1}^2/2\sigma_x^2) \\ i_{q,sx}\cos\theta_{vx} = P_{sx} \cdot exp(-\theta_{r2}^2/2\sigma_x^2) \end{cases} \tag{7}$$

It should be noted that Equation (1) can not be solved for a pixel at which strong specular reflection is

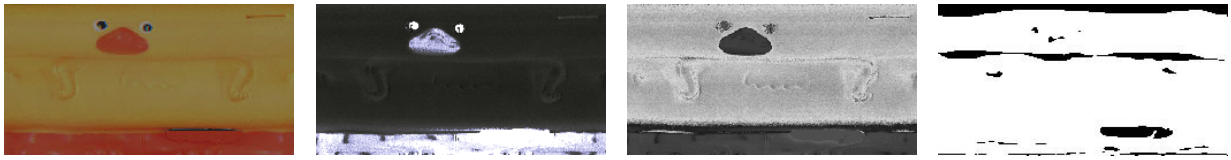

(a) Diffuse reflectance parameter (P_d) (b) Specular reflectance parameter (P_s) (c) Surface roughness parameter (σ_d) (d) Observation area for specular reflection

Figure 10: Estimated reflectance parameters for Object A.

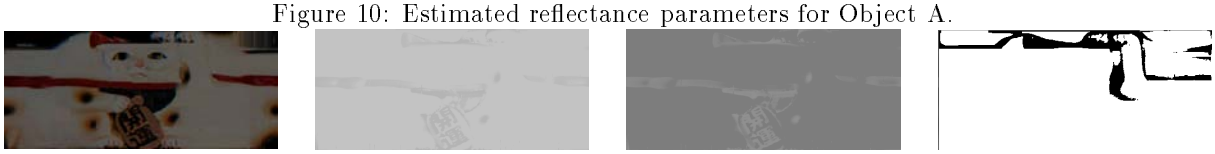

(a) Diffuse reflectance parameter (P_d) (b) Specular reflectance parameter (P_s) (c) Surface roughness parameter (σ_d) (d) Observation area for specular reflection

Figure 11: Estimated reflectance parameters for Object B.

observed less than twice. In such a case, the specular reflectance and surface roughness parameters are obtained by using a linear-interpolation method within a $W \times W$ window.

3.2 Experimental results

In order to verify our method, we have carried out experiments for densely estimating reflectance parameters of Objects A $\sim$ D in Figure 7. Note that with respect to the window size used in interpolation method, we fixed $W = 5$.

3.2.1 Estimated reflectance parameters

Estimated parameters for the objects are given in Figures 10 and 11, where parameter values are coded in color or intensity in the cylindrical coordinates. The diffuse reflectance parameter estimated over the object surface is shown in (a) of each figure. The specular reflectance and surface roughness parameters are shown in (b) and (c) of each figure, respectively. Note that all (c) in each Figure are illustrated with gray-scale where the largest value is coded as white. This image means that the smaller the value is, the smoother the object surface is. In addition, all (d) in each figure illustrates the ratio of pixels where specular reflectance and surface roughness parameters can be computed. The black part means that both parameters are not directly estimated.

In Figure 10, it is clearly shown that the specular reflectance and the surface roughness parameters of the doll's beak and leg are different from the rest. Actually, the beak and legs are highly reflective as can be seen in Figure 7(a). In Figure 11, the reflectance parameters of Object B having a more complex geometry is estimated. In this figure, it can be observed that some parts have the diffuse reflection component

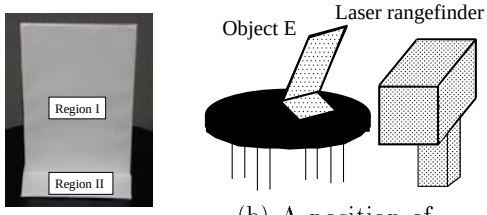

(a) Object E (b) A position of Object E

Figure 14: An object with interreflections.

and other parts have the specular reflection component as well as Object A. It is verified from these results that the non-uniform surface reflectance properties can be observed efficiently by our light selection method.

These results also show that uniform of non-uniform specular reflectance and surface roughness parameters are estimated without interpolation for more than nearly 90% of the surface.

3.3 Discussion

In this section, we have estimated non-uniform object surface reflectance properties densely by using the local illumination model (Torrance-Sparrow model). As described in Section 2, because the local illumination model considers only the direct illumination effect on the object surface, there may exist some errors in the case of occurring interreflections. In this section, we examine how much errors the proposed method inolve due to the influence of interreflections.

In the experiment, we use Object E shown in Figure 14(a), which is separated into two regions I and II. We have conducted two setups. One is that the same white paper with a uniform diffuse reflectance surface

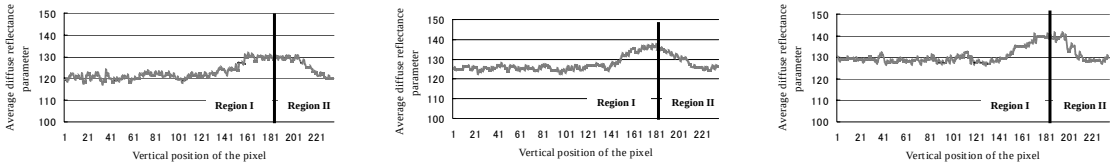

(a) R channel (b) G channel (c) B channel

Figure 12: Estimated diffuse reflectance parameter in the experimental setup 1.

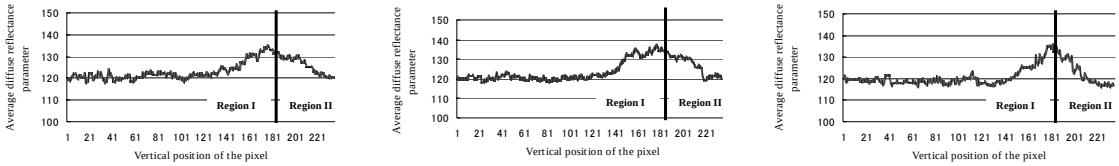

(a) R channel (b) G channel (c) B channel

Figure 13: Estimated diffuse reflectance parameter in the experimental setup 2.

is pasted up on both regions (setup1). The other is that the same glossy paper with a uniform reflectance surface is pasted up on both regions (setup2). In both setups, the Object E is put on the table obliquely as shown in Figure 14(b), so that the influence of interreflections can be observed. It is expected that, if interreflections occur, the estimated value in the inverse local rendering method must exhibit incorrect results in that part. Results for diffuse (setup1) and specular (setup2) surfaces are shown in Figures 12 and 13, respectively. Each graph represents RGB channels of the diffuse reflectance parameter estimated in both setups. The horizontal axis in the graph means the position of the surface point in the vertical direction of Object E and the vertical axis means the average of diffuse reflectance parameters in the horizontal direction of the object. In Figure 12, it is observed that the diffuse reflectance parameters estimated by the present method are large around the boundary between the regions α and β. Moreover, the influence of interreflections also remains in the glossy surface as slightly observed in Figure 13, because interreflections due to the specular reflection also occurs at the boundary between the regions I and II in the second setup. Here, in this experiments, it is actually observed that the influence of interreflections cause some errors in estimation of object surface reflectance properties.

4 Inverse Radiosity for Dense Reflectometry Estimation

4.1 Radiosity redering method

In most shading algorithms (i.e. Torrance-Sparrow model), light sources have always been treated separately from the surfaces they illuminate. In contrast, radiosity methods [8] allow any surface to emit light; thus, all light sources are modeled inherently as having area. In the radiosity method, the environment is breaked up into a finite number γ of discrete patches, each of which is assumed to be of finite size, emitting and reflecting light uniformly over its entire area. If we consider each patch to be an opaque Lambertian diffuse emitter and reflector, then, for surface u,

$$B_u = E_u + P_{du} \sum_{v=1}^{\alpha} B_v F_{uv}, \qquad (8)$$

where B_u and $B_v (1 \leq u, v \leq \gamma)$ are the radiosities of patches u and v, measured in energy/unit time/unit area(i.e., W/m^2). Note that γ is the number of object patches. E_u is the rate at which light is emitted from patch u and has the same units as radiosity. P_{du} is patch u's reflectivity and is dimensionless.

F_{uv} is called the dimensionless *form factor*, which specifies the fraction of energy leaving the entirety of patch v that arrives at the entirety of patch u, taking into account the shape and relative orientation of both patches and the presence of any obstructing patches.

4.2 Estimation of surface reflectance parameters with considering diffuse interreflections

Since the object is measured in a dark room in the present study, we can assume that the influence of environment light can be ignored. In other words, the form factor between each patch of the object and the wall of the dark room need not be calculated.

Here, recall that Figure 1 shows a general flow diagram of estimating surface reflectance properties in our method. The proposed method consists of four

parts. The first three processes (A, B and C) have already been described in Section 2, which represent measurement of an object (A and C), selection of light source (B), respectively. In this section, process (D) is constructed of the *inverse radiosity rendering* for estimating the diffuse reflectance parameter, and the estimation of the specular reflectance and surface roughness parameters using the Torrance-Sparrow model.

4.2.1 Estimation of diffuse reflectance parameter based on radiosity

In the proposed method, the hemi cube method [4] can be used for calculating the form factor F_{uv} because the object shape has already been measured by the laser rangefinder. Since the range and texture images are registered at each pixel, the radiosity B_u of the patch u is calculated based on the sum of the values of the pixels which correspond to the patch u. Here, P_{du} represents the diffuse reflectance parameter on the patch u. Then, the diffuse reflectance parameter P_{du} is determined as follows:

$$P_{du} = \frac{B_u - E_u}{\sum_{v=1}^{\alpha} B_v F_{uv}}, \quad (9)$$

where E_u is 0 since there is no emission at the patch u on the object. Finally, the diffuse reflectance parameter at each surface point is estimated by calculating the average among neighbouring patches which share the point.

Here, we describe the calculation of the radiosity B_u of the patch u in more detail. Each patch consists of four points and B_u is represented as the sum of the color values of the pixels which correspond to these points. Let us suppose that the patch u contains pixels s and t. It should be noted that pixel values e_s and e_t of s and t in T_{diff} are obtained with different light positions $p(s)$ and $p(t)$, respectively, because the light source attached with the rangefinder moves during measurement (Figure 15). In calculating the B_u, it is required to use the color value $\widehat{e_t}$ of the pixel t with the light position $p(s)$. From the Lambert's law,

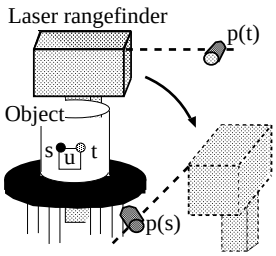

Figure 15: Calculation of radiosity.

the color value $\widehat{e_t}$ can be obtained by:

$$\widehat{e_t} = \frac{\mathbf{N}_t \cdot \mathbf{L}_{p(s)t}}{\mathbf{N}_s \cdot \mathbf{L}_{p(s)s}} e_s, \quad (10)$$

where $\mathbf{N}_s$ and $\mathbf{N}_t$ are normal vectors at pixels s and t. $\mathbf{L}_{p(s)s}$ and $\mathbf{L}_{p(s)t}$ are light vectors with the light position $p(s)$ at pixels s and t. Note that in the case of $\mathbf{N} \cdot \mathbf{L} \leq 0$, the color value $\widehat{e_t}$ should be 0 to consider the measurability of light reflection.

4.2.2 Estimation of specular reflectance and surface roughness parameters based on Torrance-Sparrow model

The specular reflectance and the surface roughness parameters are estimated by using the Torrance-Sparrow model in Section 2. The specular reflectance parameter P_{sx} and the surface roughness parameter σ_x at the surface point x are estimated by solving the simultaneous equation. In this case, we use the pixel values of the specular reflection component extracted from two images taken under two different illumination conditions and P_{dx} estimated previously.

4.3 Experimental results

In the experiment, we use five objects: Objects A $\sim$ E already used in previous sections. Here, Object E is used in a preliminary experiment for demonstrating that our inverse radiosity method can eliminate the influence of diffuse interreflections. Note that with respect to the window size used in interpolation method, we fixed $W = 5$.

This experiment is conducted to confirm the effect of eliminating the influence of interreflections. We separate Object E, having a right-angled fold into two regions I and II as shown in Figure 7(a). For this experiment, we also used two setups exactly the same as in Section 3.3. In one setup, a white paper having a uniform diffuse reflectance surface was pasted to both regions (setup 1). In the second setup, glossy paper having a uniform reflectance surface was pasted to both regions (setup 2). Then, we compare our inverse radiosity method with our previous method [17, 16, 18] described in the last section, which does not consider interreflections in estimating reflectance parameters. If interreflections occur, the estimated value in the previous method should be incorrect in that part. The results for diffuse (setup 1) and specular (setup 2) surfaces are shown in Figures 16 and 17, respectively. Each graph represents RGB channels of the diffuse reflectance parameter estimated by both methods. The horizontal axis indicates the position of the surface point in the vertical direction of Object E, and the vertical axis indicates the average

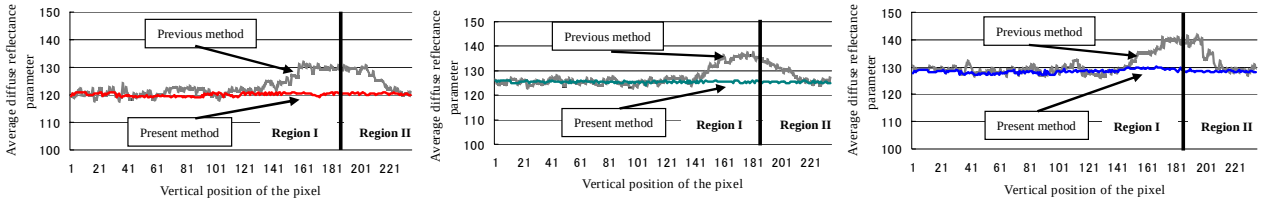

(a) R channel (b) G channel (c) B channel

Figure 16: A comparison with previous works for Object E with diffuse surfaces.

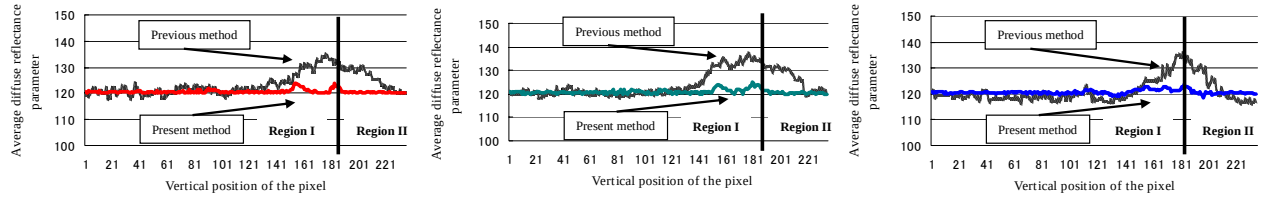

(a) R channel (b) G channel (c) B channel

Figure 17: A comparison with previous works for Object E with glossy surfaces.

(a) Object A (b) Object B

Figure 18: Difference between estimated diffuse reflectance parameters with inverse radiosity and with the method in Section 3.

of diffuse reflectance parameters in the horizontal direction. Figure 16 shows that the diffuse reflectance parameters estimated by the previous method are large around the boundary between regions I and II. In contrast, such an effect is rather reduced in the present method. This clearly shows the effectiveness of the inverse radiosity method. However, the influence of interreflections still remains slightly in the glossy surface, as can be observed in Figure 17, because interreflections due to the specular reflection also occur at the boundary between regions I and II in the second setup. The diffuse reflectance parameter obtained by the present method looks smoother than that obtained by the previous method. This is because the diffuse reflectance parameter of a point on the object is calculated as the average of the diffuse reflectance parameters of four patches that share the point.

4.3.1 Estimated reflectance parameters

The next experiment was conducted in order to examine the effect of considering interreflections in reflectance parameter estimation of non-uniform objects: Objects A and B. Figures 18(a) and (b) illustrate the sum of differences in RGB channels of the diffuse reflectance parameters between the previous and present methods. These images are shown using cylindrical coordinates in gray-scale having a maximum value of 255. The difference is large in parts in which interreflections occur. These results show that the present method is effective for objects that have non-uniform surface reflectance properties and exhibit interreflections. Some parts have larger differences than others. For example, the part of the beak of Object A and the arms and legs in Object B. In the inverse radiosity method, the diffuse reflectance parameter is calculated as the average of four patches, as explained in preliminary experiments. Therefore, the diffuse reflectance parameter that includes the influence of specular interreflections is also smoothed, this smoothing process causes a large difference compared to the previous method.

The part where the color squre surrounds in Figure 19 shows difference of result between the inverse local rendering and the inverse rendering. For example, the diffuse reflection component is different between left and right image in (a). The rendering result of

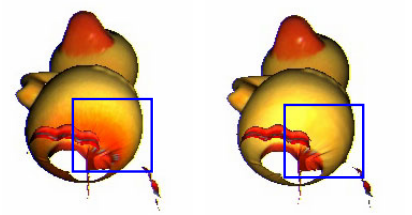

Inverse local rendering Inverse radiosity rendering

(a) Object A

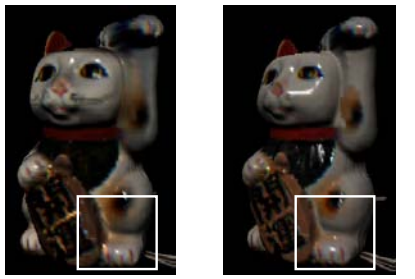

Inverse local rendering Inverse radiosity rendering

(b) Object B

Figure 19: Difference of rendering results based on the inverse radiosity rendering and with the inverse local rendering in Section 3.

inverse radiosity rendering shows the diffuse interreflections are removed with comparing to the result of the inverse local rendering. (b) is also clear that an influence of diffuse interreflections are eliminated.

5 Inverse Photon Mapping for Dense Reflectometry Estimation

5.1 Photon mapping

In the photon mapping rendering method [9], an outgoing radiance L from a surface point x is calculated to decide a surface color. The following equations form the rendering equations in the photon mapping method.

$$L(x, \vec{\omega}) = L^e(x, \vec{\omega}) + L^r(x, \vec{\omega}), \tag{11}$$

$$L^r(x, \vec{\omega}) = \int_\Omega f(x, \vec{\omega}', \vec{\omega}) L^o(x, \vec{\omega}')(\vec{\omega}' \cdot \vec{n}) d\vec{\omega}', \tag{12}$$

x	:	Surface point
$\vec{n}$	:	Unit vector of surface normal at x
$\vec{\omega}$	:	Direction from outgoing radiance
$\vec{\omega}'$	:	Direction of incoming radiance
$d\vec{\omega}$	:	Differential solid angle
Ω	:	Hemisphere of directions

where $L^e(x, \vec{\omega})$, $L^r(x, \vec{\omega})$, $L^o(x, \vec{\omega}')$ and $f(x, \vec{\omega}', \vec{\omega})$ represent the emitted radiance, the reflected radiance, the incoming radiance, and a BRDF (i.e. the Torrance-Sparrow model), respectively.

5.2 Estimation of surface reflectance parameters with considering both diffuse and specular interreflections

Here, the outgoing radiance L in Equation (11) is equivalent to the reflected radiance L^r due to the assumption that the underlying objects have no emission. Equations (11) and (12) are theoretical models. In fact, the color $\widehat{i_x}$ at a surface point x is represented by the following equation called Ward reflectance model using Equation (1) [27].

$$\begin{aligned} \widehat{i_x} &= I_x\{\frac{P_{dx}}{\pi} + P_{sx}\frac{exp(-tan^2\theta_{rx}/\sigma_x^2)}{4\pi\sigma_x^2}\} \\ &= I_x\{\frac{P_{dx}}{\pi} + P_{sx}K(\theta_{vx}, \theta_{rx}, \sigma_x)\}, \end{aligned} \tag{13}$$

where I_x is the incoming radiance. $K(\theta_{vx}, \theta_{rx}, \sigma_x)$ denotes the specular term in Equation (1), and other parameters are the same as in Equation (1). In practice, the Ward model described above has five parameters for representing an anisotropic object surface reflectance properties. Because we assume that the object has isotropic reflectance properties, unknown parameters are three (the diffuse reflectance, the specular reflectance and the surface roughness parameters). I_x is decided by counting the number of photons which arrive at the point x. The photon is specifically traced by a Monte Carlo ray tracing method [10]. In this case, the photon is reflected or absorbed according to the reflectance parameters, and only the photon which is reflected is traced iteratively.

Figure 20 illustrates the detail of iterative reflectance estimation process based on inverse photon mapping. The reflectance parameter estimation method based on inverse photon mapping is separated into two processes (a) and (b). These processes are conducted iteratively. In each process, we minimize the following equation derived from Equation (13) at each pixel in the texture image.

$$E(P_{dx}, P_{sx}, \sigma_k) = \sum_{j=1}^{q}(i_{xj} - \widehat{i_{xj}})^2, \tag{14}$$

where i_{xj} is the measured radiance (color intensity), and $\widehat{i_{xj}}$ is the irradiance which is computed from Equation (13) at the surface point x with light source position j. q denotes the number of sample points.

In the process (a), the diffuse reflectance parameter P_{dx} is estimated by using a pixel which is categorized as T_{diff}. P_{dx}^{init}, P_{sx}^{init} and σ_x^{init} are used to compute

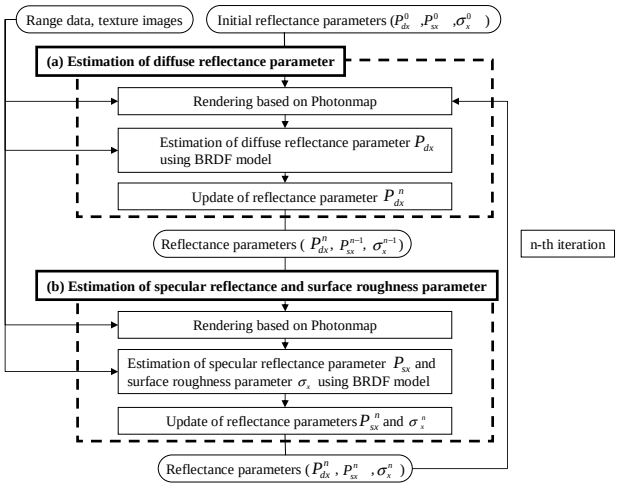

Figure 20: Detail of reflectance estimation process based on inverse photon mapping.

$\widehat{i_{xj}}$ only at the first iteration. Here, the specular reflection term in Equation (13), $I_x P_{sx} K(\theta_{vx}, \theta_{rx}, \sigma_x)$, is set to be 0 because the specular reflection can not be observed.

In the process (b), the specular reflectance P_{sx} and the surface roughness σ_x parameters are estimated by using only pixels categorized as T_{spec} and T_{none}. P_{sx}^{init} and σ_x^{init} are used again to compute $\widehat{i_{xj}}$ only at the first iteration. P_{dx} estimated above is used in Equation (13). When P_{sx} and σ_x are estimated, the value of each reflectance parameter is updated and the processes (a) and (b) are iterated th_2 times. The reflectance parameter is selected when differences between the real and synthetic images is the minimum value among th_2 samples. Because this is non-linear equation with some unknown parameters, we iteratively perform the photon mapping rendering and estimation of surface reflectance parameters, and minimize the difference between the real image and synthesis image (Equation (14)). To minimize this equation, there are some methods such as downhill simplex method [3]. We also employ downhill simplex algorithm for this minimization problem.

After the estimation process finishes, the specular reflectance and the surface roughness parameters may not have a correct value, if the specular reflection component is significantly small. Such parameters are interpolated linearly by scanning the texture image horizontally.

5.3 Experimental results

In Section 3 and 4, we have already proposed two methods of inverse reflectometry (hereafter called the method I and the method II). In the following, we first show the result of comparing estimated reflectance parameters by the present method (hereafter called the method III) with the methods I and II using Object E. We then examine the effect of considering interreflections in surface reflectance parameter estimation using Objects A $\sim$ D with uniform and non-uniform surface properties. Finally, we show rendered images based on reflectance parameters estimated by using the method III. See Figure 7 and 14 for the test objects used in the expriments. The number of photons is 2 million and our algorithm requires approximately 4 hours to estimate the reflectance parameters of each object. The threshold is fixed $th_2 = 50$.

5.3.1 Preliminary experiments

In preliminary experiments, we demonstrate the performance of the present method using a simple object (Object E). Especially we compare the present method III with the previous methods I (with no consideration of interreflections described in Section 3) and II (with consideration of only diffuse interreflections described as Section 4). Object E consists of two plates (region I and II) which are adjacent with 90 degrees mutually. We also used two experimental setups exactly the same as in Section 3.3. Results are shown in Figures 21 for setup 1 and 22 for setup 2. Each graph represents RGB channels of the diffuse reflectance parameter estimated by three methods. A horizontal axis represents the position of the pixel along the vertical direction of the object and a vertical axis represents the average of diffuse reflectance parameters along the horizontal direction of the object. In the methods I and II, the value of the diffuse reflectance parameter is large around the boundary between regions I and II due to the influence of interreflections. On the other hand, in the present method, the parameter estimated is more stable. From these results, it is clear that the present method III can eliminate the influence of both diffuse and specular interreflections.

5.3.2 Estimated reflectance parameters

In the next experiment, we use Objects A $\sim$ D shown in Figures 7. These objects have non-uniform or uniform diffuse and specular reflectance properties.

Figure 23 and 24 show the cylindrical images of real objects and difference images between real and synthetic images (rendered by photon mapping) in the method II and the present method III for each test object (Object C and D), respectively. The light position locates at the above on the rangefinder. Synthetic images are rendered using estimated reflectance parameters under the same illumination

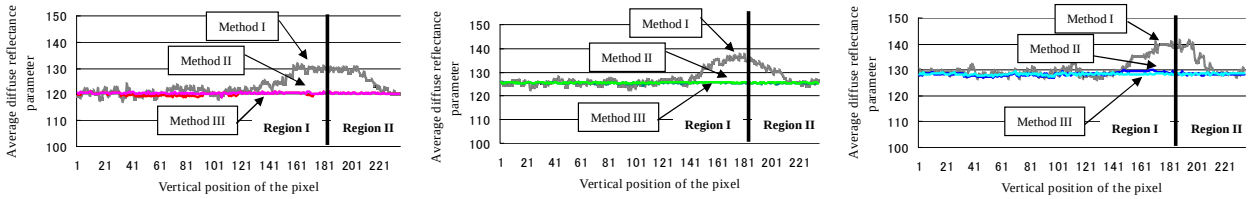

(a) R channel (b) G channel (c) B channel

Figure 21: A comparison among three methods for Object E with dffuse surfaces.

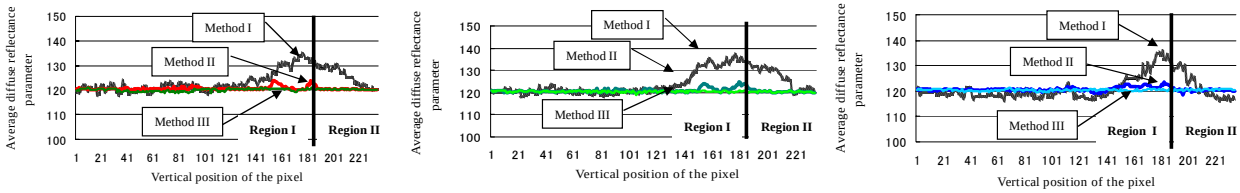

(a) R channel (b) G channel (c) B channel

Figure 22: A comparison among three methods for Object E with glossy surfaces.

condition as in the real images. Note that linear interpolation is conducted when the specular reflectance and the surface roughness parameters can not be estimated due to small value of the specular reflection. In the previous method II, the error due to the influence of specular interreflections is confirmed. Especially, Objects C and D exhibit large errors at the part of inequalities (i.e. cats' leg, neck, and pigs' nose). The present method III does not have such an influence. Additionally, Table 2 shows the variance of differences between real and synthetic images. The present method III has much smaller variances than the method II for all the objects. These results show the present method III can accurately estimate each reflectance parameter even if diffuse and specular interreflections occur.

Figure 25 shows the relationship between the iterated process and the differences between real and synthetic images. The vertical axis indicates the sum of differences between the real and synthetic images, and the horizontal axis indicates the number of iterations. Each graph shows that the iterated estimation process decreases the difference between real and synthetic images. However, the minimum difference may not be the global minimum because the proposed iteration method ends when the number of iterations reaches 50. Therefore, each graph illustrates pulsation of the differences. In other words, the higher the number of iterations, the lower the differences.

5.3.3 Rendering results with the photon mapping method

Figure 26 shows rendered images of Object C and D based on reflectance parameters estimated by the *inverse photon mapping rendering*. It is clear that these images are photorealistically rendered. However, there are some errors with respect to the geometry. For example, some parts of pig's legs (a) are not rendered and there are spike noises at cat's legs (b). These errors are due to noise in range images. To solve this problem, it is necessary to interpolate the range data using the data around these parts.

6 Conclusions

The objective of this study is to develop a new surface reflectance modeling method which can densely estimate non-uniform reflectance properties for almost the whole object surface by using the laser rangefinder for virtualizing real objects.

At the beginning of the study, multiple light source positions around the laser rangefinder are automatically selected, so that both diffuse and specular reflection components are observed densely. In experiments, we show that our approach can discriminately observe the diffuse and specular reflection components on the object surface. But, even when our approach is performed, it is difficult to observe both reflection components on the whole object surface. Therefore, it is necessary to plan the lighting conditions in the scene to observe the reflection components densely. We then have proposed three methods for surface reflectance estimation based on *inverse rendering* framework without assumption of uniform object surface reflectance properties.

In future work, we will extend the following items.

- Light planning in observing the object surface reflection component.
- Automatic estimation of scene lighting conditions.

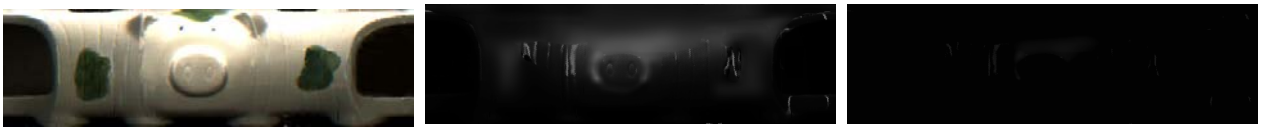

(a) Real image (b) Difference between real and synthetic images (method II) (c) Difference between real and synthetic images (method III)

Figure 23: Differences between real and synthetic cylindrical images for Object C.

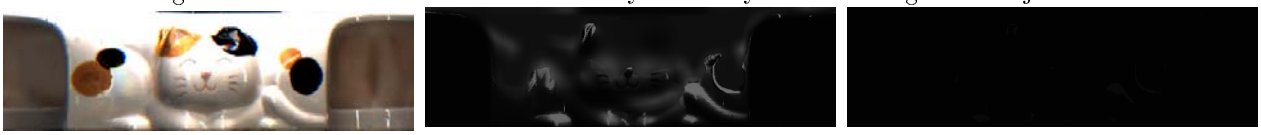

(a) Real image (b) Difference between real and synthetic images (method II) (c) Difference between real and synthetic images (method III)

Figure 24: Differences between real and synthetic cylindrical images for Object D.

Table 2: Average and variance of differences between real and synthetic images.

		Object A	Object B	Object C	Object D
Average	Method II	17.7	20.1	8.7	13.3
	Method III	1.11	1.06	0.51	0.92
Variance	Method II	501.9	485.4	493.3	375.2
	Method III	6.8	8.0	3.2	9.8

- Real time estimation by using graphics hardware.

The first item can improve the light selection method to observe both object surface reflection components more accurately and densely. The second item helps us to merge the virtual and virtualized objects into the real world. Because our method can estimate object reflectance parameters, it is easy to faithfully represent the object if the lighting condition is known. The third item is concerned with rapid estimation by implementing the algorithm on high speed graphics hardware (GPU). Photon mapping rendering is already implemented on GPU in resent other researches. Therefore, by using these methods, our estimation processes can be done in real time. Real time estimation has grateful usefulness in computer vision and graphics. If three items described above are achieved, the proposed technique can be practically applied to a number of fields such as mixed reality.

References

[1] R. T. Azuma. A Survey of Augmented Reality. *Presence*, Vol. 6(No. 4):355–385, 1997.

[2] R. Baribeau, M. Rioux, and G. Godin. Color Reflectance Modeling Using a Polychromatic Laser Sensor. *IEEE Trans. on Pattern Analysis and Machine Intelligence*, Vol. 14(No. 2):263–269, 1992.

[3] S. Boivin and A. Gagalowicz. Image-Based Rendering of Diffuse, Specular and Glossy Surfaces from a Single Image. *Proc. ACM SIGGRAPH '01*, pages 107–116, August 2001.

[4] M. F. Cohen, D. P. Greenberg, D. S. Immel, and P. J. Brock. An Efficient Radiosity Approach for Realistic Image Synthesis. *IEEE Trans. on Computer Graphics and Application*, Vol. 6(No. 3):26–35, 1986.

[5] J. Foley, A. van Dam, S. Feiner, and J. Hughes. *Computer Graphics Principles and Practice.* Addison-Wesley Publishing Company, 2nd edition, 1993.

[6] A. Fournier, A. S. Gunawan, and C. Romanzin. Interactive Common Illumination for Computer Augmented Reality. *Proc. Int. Conf. on Graphics Interface (GI1993)*, pages 254–262, May 1993.

[7] K. Ikeuchi and K. Sato. Determining Reflectance Properties of an Object Using Range and Brightness Images. *IEEE Trans. on Pattern Analysis and Machine Intelligence*, Vol. 13(No. 11):1139–1153, 1991.

[8] D. S. Immel, M. F. Cohen, and D. P. Greenberg. A Radiosity Method for Non-diffuse Environments. *Proc. ACM SIGGRAPH '86*, pages 133–142, 1986.

[9] H. W. Jensen. *Realistic Image Synthesis Using Photon Mapping.* A K Peters, Ltd, 1st edition, 2001.

[10] J. T. Kajiya. The Rendering Equation. *Proc. ACM SIGGRAPH '86*, pages 143–150, August 1986.

[11] G. Kay and T. Caelli. Inverting an Illumination Model from Range and Intensity Maps. *CVGIP: Image Understanding*, Vol. 59(No. 2):183–201, 1994.

[12] S. Lin and S. W. Lee. A Representation of Specular Appearance. *Proc. 7th IEEE Int. Conf. on Computer Vision*, Vol. 2:849–854, 1999.

[13] S. Lin and S. W. Lee. Estimation of Diffuse and Specular Appearance. *Proc. 7th IEEE Int. Conf. on Computer Vision*, Vol. 2:855–860, 1999.

[14] C. Loscos, G. Drettakis, and L. Robert. Interactive Virtual Relighting of Real Scenes. *IEEE Trans.*

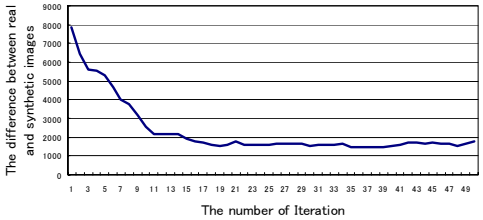

(a) Object C

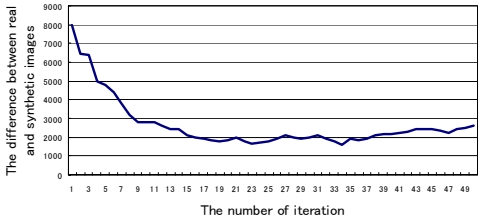

(b) Object D

Figure 25: Relationship between the number of iterations and difference between real and synthetic images for Objects C and D.

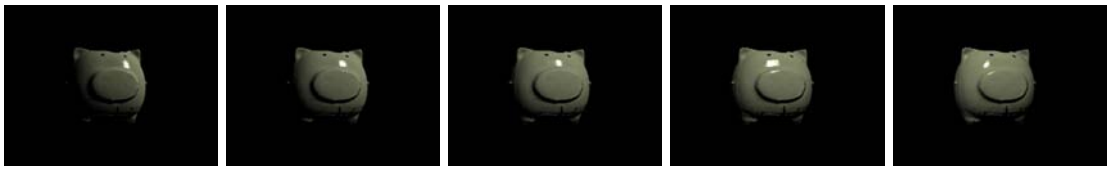

(a) Rendering results of Object C

(b) Rendering results of Object D

Figure 26: Rendering results of Object C and D under arbitrary illumination conditions.

Visualization and Computer Graphics, Vol. 6(No. 4):289–305, December 2000.

[15] J. Lu and J. Little. Reflectance Function Estimation and Shape Recovery from Image Sequence of a Rotating Object. *Proc. 5th IEEE Int. Conf. on Computer Vision*, pages 80–86, June 1995.

[16] T. Machida, H. Takemura, and N. Yokoya. Dense Estimation of Surface Reflectance Parameters by Selecting Optimum Illumination Conditions. *Proc. 14th Int. Conf. on Vision Interface (VI2001)*, pages 244–251, June 2001.

[17] T. Machida, H. Takemura, and N. Yokoya. Dense Estimation of Surface Reflectance Parameters from Registered Range and Color Images by Determining Illumination Conditions. *Proc. SPIE Electronic Imaging*, pages 127–134, January 2001.

[18] T. Machida, H. Takemura, and N. Yokoya. Dense Estimation of Surface Reflectance Properties for Merging Virtualized Objects into Real Images. *Proc. 5th Asian Conf. on Computer Vision (ACCV2001)*, pages 688–693, January 2002.

[19] T. Machida and N. Yokoya. Dense Estimation of Surface Reflectance Properties of Objects with Interreflections. *Proc. 16th IEEE Int. Conf. on Pattern Recognition (ICPR2002)*, pages 348–351, August 2002.

[20] T. Machida and N. Yokoya. Virtualizing Real Objects with Surface Interreflections. *Proc. IEEE Int. Conf. on Multimedia and Expo (ICME2002)*, pages 833–836, August 2002.

[21] T. Machida, N. Yokoya, and H. Takemura. Surface Reflectance Modeling of Real Objects with Interrefletions. *Proc. 9th IEEE Int. Conf. on Computer Vision (ICCV2003)*, pages 170–177, October 2003.

[22] T. J. Purcell, I. Buck, W. R. Mark, and P. Hanrahan. Ray Tracing on Programmable Graphics Hardware. *ACM Trans. on Graphics*, pages 703–712, 2002.

[23] T. J. Purcell, C. Donner, M. Cammarano, H. W. Jensen, and P. Hanrahan. Photon Mapping on Programmable Graphics Hardware. *Proc. Graphics Hardware*, pages 265–272, 2003.

[24] I. Sato, Y. Sato, and K. Ikeuchi. Acquiring a Radiance Distribution to Superimpose Virtual Objects onto a Real Scene. *IEEE Trans. on Visualization and Computer Graphics*, Vol. 5(No. 1):1–12, January 1999.

[25] Y. Sato, M. D. Wheeler, and K. Ikeuchi. Object Shape and Reflectance Modeling from Observation. *Proc. ACM SIGGRAPH '97*, pages 379–387, 1997.

[26] K. E. Torrance and E. M. Sparrow. Theory for Off-specular Reflection from Roughened Surfaces. *Journal of the Optical Society of America*, Vol. 57(No. 9):1105–1114, 1967.

[27] G. J. Ward. Measuring and Modeling Anisotropic Reflection. *Proc. ACM SIGGRAPH '92*, pages 265–272, July 1992.

[28] N. Yokoya and M. D. Levine. Range Image Segmentation Based on Differential Geometry: A Hybrid Approach. *IEEE Trans. Pattern Analysis and Machine Intelligence*, Vol. 11(No. 6):643–649, June 1989.

[29] Y. Yu, P. E. Debevec, J. Malik, and T. Hawkins. Inverse Global Illumination: Recovering Reflectance Models of Real Scenes from Photographs. *Proc. ACM SIGGRAPH '99*, pages 215–227, August 1999.